Journal of Materials Chemistry A

Accepted Manuscript

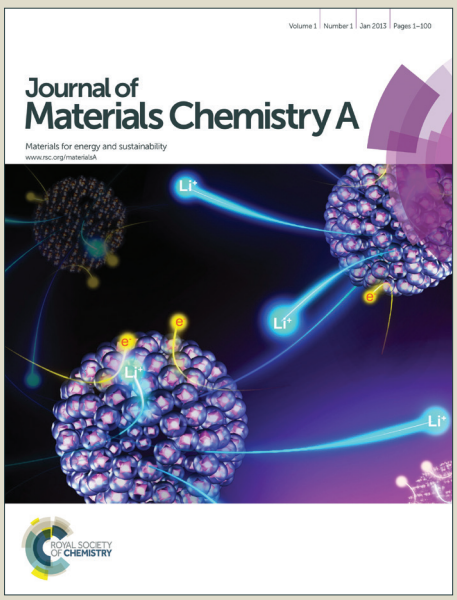

ROYAL SOCIETY OF CHEMISTRY

www.rsc.org/materialsA

Journal of
Materials Chemistry A

RSCPublishing

PAPER

Fabrication of porous graphene/polyimide composites using leachable poly-acrylic resin for enhanced electrochemical and energy storage capabilities.

Cite this: DOI: 10.1039/x0xx00000x

Received on
Accepted on

DOI: 10.1039/x0xx00000x

www.rsc.org/

Patricia Azuka Okafor[a], Jude O. Iroh[b]

Specific capacitance of graphene-polyimide composites is significantly enhanced by incorporation of porous structures in the polymer composite. The selective decomposition of thermally labile poly-acrylic resin introduced into the composite during synthesis creates pores of varying size and shapes. It is noted that samples synthesized with lower weight percent acrylic polymer produced more uniform sized pores than those with higher weight percent. The presence of pores increased available surface area of the stacked graphene sheets available for ion adsorption and double layer formation. Scanning electron miscroscope (SEM) images confirms the presence of pores and reveals filler orientation around porous regions. Cyclic voltammetry (CV) show an increase in specific capacitance from 39 F/g to 133 F/g and electrochemical impedance spectroscopy (EIS) shows significant decrease in bulk resistance and a 100% increase in theoretical porosity when tested in 0.4M potassium hexaflorophosphate VI (KPF6)/propylene carbonate electrolyte solution. Shifts in imide peaks to lower wave numbers in Raman and Fourier transform spectroscopy (FTIR) suggests presence of chemical interaction between filler and matrix confirming uniform dispersion of fillers in the material. Thermogravimetric analysis (TGA) shows thermal stability for the composite systems at temperatures above 700°C. The material is investigated for use in super capacitor applications especially in devices which require high end-use temperatures.

1. Introduction

The growing demand for hybrid and electric powered vehicles has resulted in an increased interest in electrochemical capacitors. Electrochemical capacitors also commonly known as supercapacitors are electrochemical energy storage devices that provide high power density and remarkable energy at short times. This characteristic has generated a significant interest in its application in in electric vehicles, backup power systems, and electronic components. Energy stored is based on the formation of an electric double layer at the interface between an electronically conductive material and an electrolyte solution; or by fast and reversible faradic reactions (pseudocapacitors); these mechanisms can function simultaneously, depending on the nature of the electrode material. [1–3]. Activated carbons (ACs), nanostructured metal oxides like ruthenium oxide, iridium oxide, manganese oxide and conducting polymers like polyaniline, polythiophene, polypyrrole have been the most widely used electrode materials for super capacitors due to their remarkable high capacitance values ~ > 200-800 F/g However, factors such as high costs, poor cycle stability, low flexibility remains a major drawback [4-5].

Recently, graphene has been explored as ideal candidate for high power and high energy density electrode material due to its high electrical and thermal conductivity, good flexibility and high surface area. Mono layer graphene deposited on transition metal substrate via chemical vapor deposition (CVD) methods yields defect free graphene with high charge carrier concentrations of up to 1013 cm^{-2} and room temperature mobility of ~10000 $cm^{-2}s^{-1}$ [10-12]. Graphitic electrodes have shown enhanced electron transport rates, improved

cyclabilities, and higher sensitivities to reactions [10-11]. In the last couples of years, graphene has been used as an alternative carbon-based nanofiller in the preparation of polymer nanocomposites and have shown improved mechanical, thermal, and electrical properties [12-13].

The growing interest in composite material in electrode applications is due to their availability, low cost, thermal stability and environmental friendliness. Graphene based polymer nanocomposites possess much higher active material utilization ratios and superior ultrafast charge and discharge ability [13,14]. Murugan et al [14] synthesized a graphene/PANI composite containing 50wt% graphene with an overallc double layer capacitance and psuedo-capacitance of 408F/g. However, due to poor stability of polyaniline at ambient condition, cycle stability and lifetime is limited. Other polymers like polystyrene, polytetraflouroethylene (PTFE), e.t.c [4, 11] have been used for molecular dispersion of chemically modified graphene (CMG) sheets in producing high performance electrodes. Polyimides, a useful class of polymers is recently been explored as matrix for dispersing graphene due to their high chemical and thermal stability (stable up to 750^{o}C), high optical transmission and high mechanical strength. They are a suitable matrix for incorporation of metal, salts, carbon materials and chromophores as nanoscale particles to obtain of nanocomposite materials [15-16]. Graphene-polyimide nanocomposites have the combined superior properties of graphene and polyimide [17]. The superior electrical and the extremely large surface area of graphene and the excellent mechanical and thermal stability of polyimide makes this nanocomposite material a strong contender for use in energy storage, supercapacitors, fuel cell, solar energy, electronic display devices and biosensors [7,17-18]. Extensive research has been carried out to study the electrical, thermal and mechanical properties of graphene-polyimide composites [10, 16, 20-21], however not much work has been published on its electrochemical and energy storage capabilities.

Graphene-polyimide composites exhibit poor electrochemical properties due to the rigid structure of the composite restricting diffusion pathways of electrolyte ions resulting in decreased capacitance [15]. Aliphatic polyimide precursors usually yield less rigid polyimides with better chain flexibility however, they are not as reactive as aromatic polyimide precursors. Yuena meng el at [19] recently synthesized flexible graphene-polyimide using aliphatic (ethylene diamine) and an aromatic dianhydride (PMDA) precursors in the presence of interconnected macroporous graphene fillers. The hierarchical structure of graphene in the composite system results in low resistances for the reaction of lithium ions during battery testing yielding specific capacity values as high as 175mAh/g when tested in 1M lithium electrolyte solution.

In this work, aromatic polyimide precursors, 4, 4' oxydianiline (ODA) and pyromellitic dianhydride (PMDA) are used as starting matrix in the presence of 50wt% nano-graphene sheets (50-100nm layers) to synthesize graphene-polyimide composite films. The resulting composite is a very stiff material with a high glass transition temperature (Tg) of ~ 440^{o}C and storage modulus of 7.20GPa [39]. The material's rigidity limits ion permeation through the bulk and hence, reduces contact between embedded graphene fillers and electrolyte ions during electrochemical testing. Theoretically, it's been shown that ion adsorption on graphene surfaces/edges yields specific capacitance as high as 550 F g^{-1} when all the surface is used [8]; this becomes a unique possibility if all the embedded graphene surface within the polymer matrix is available for ion adsorption. To improve graphene filler contact with electrolyte ions, we introduce a thermally labile flexible poly-acrylic resin with a molecular weight of 100,000g/mol., Tg of 30^{o}C and viscosity of 0.105N.s/m^2 into the composite during synthesis. Poly-acrylic resin is chosen due to its low viscosity which enhances processability and miscibility with composite during sysnthesis. Selective degradation of the resin during curing/thermal annealing creates pores, deep gashes and crevices on the material surface which exposes embedded graphene fillers to electrolyte ions thereby creating more available adsorption sites for double layer formation. The ability of the resin to gradually unzip/degrade during the imidization process of polyimide ensures that it is leached out in a systematic manner during the imide ring closure thereby leaving distributed porous regions on the film. Proper control over pore size and specific surface area is required to ensure good performance in terms of both power delivery rate and energy storage capacity [6, 21].

To aid in analysis, neat graphene-polyimide composite synthesized without the poly-acrylic resin is compared with graphene-polyimide composites synthesized with varying weight fractions of the resin (1wt%, 5wt% and

20wt%). We report remarkable improvement in specific capacitance (up to 250% increase) and specific capacity (up to three orders of magnitude) in the porous samples compared to the neat composite. It is noted that samples synthesized with lower weight fraction of acrylic polymer showed better overall performance due to uniform distribution of pores in the system and better filler orientation. This novel method leaves room for optimization and design of similar composite materials for high electrode performance. Several electrochemical techniques including cyclic charge discharge (CCD), cyclic voltammetry (CV) and electrochemical impedance spoectroscopy (EIS) is used to study electrochemical behavior of the composite material. BET experiment is used to calculate surface area, SEM is used to study morphology of the composites. Raman spectroscopy, Fourier transform spectroscopy (FTIR) and Xray diffraction (XRD) is used to study graphene structure as well as filler-matrix interfacial properties. Surface elemental composition is studied using Xray photospectroscopy (XPS).

2. Experimental

2.1 Materials

The reagents used in this study are: nano-graphene sheets (98.48% purity) with thickness 50-100nm and length 7μm purchased from Angstron materials, Dayton, Ohio. Pyromellitic dianhydride (PMDA) (99% purity), 4, 4-oxydianiline (ODA) and *N*-methyl-pyrrolidone (99% purity) purchased from Sigma–Aldrich company and Poly-acrylic resin with a glass transition temperature of 30ºC and viscosity of 105cP obtained from Mallard creek Polymers Inc.

2.2 Synthesis of porous graphene/PI films

0.05g, 0.227g and 1.07825g corresponding to 1wt%, 5wt% and 20wt% of poly-acrylic resin is added to a round-bottom flask containing 100 mL of *N*-methyl pyrrolidone (NMP) and mechanically stirred for 15 minutes, 5.1608 g of 4, 4-oxydianiline (ODA) is added to the stirring mixture followed by steady mechanical stirring for 30 minutes. 10.782 g (50wt %) of nano-graphene powder is added to the mixture in a gradual steady manner and stirring speed increased. After 8 hours of stirring, 5.6216 g of pyrromellitic dianhydride (PMDA) is added to the mixture and mechanical stirring continued for another 12 hours while the temperature is maintained at 10 °C via a temperature bath. The experiment is carried out in an inert atmosphere with a steady purge of nitrogen gas. The same procedure is employed to synthesize the neat sample (0wt% sample) without the addition of poly-acrylic resin.

Free standing films are prepared by traditional solution casting method. The composite mixture is cast onto a clean glass substrate and thermally imidized in a step-wise manner using a Fisher scientific iso-temp vacuum oven with pressure 100psi (model 281A) at 120 °C for 2 hours, 200 °C for 1 hour, 250 °C for 1 hour and 300ºC for 4 hours. The cast films are delaminated using a sharp blade and are stored in transparent bags. The samples are named: neat sample (0%PA), 1 wt% sample (1%PA), 5wt% sample (5%PA) and 20wt% samples (20%PA). Figure 1a shows an illustration of the synthesis and preparation of the composite film.

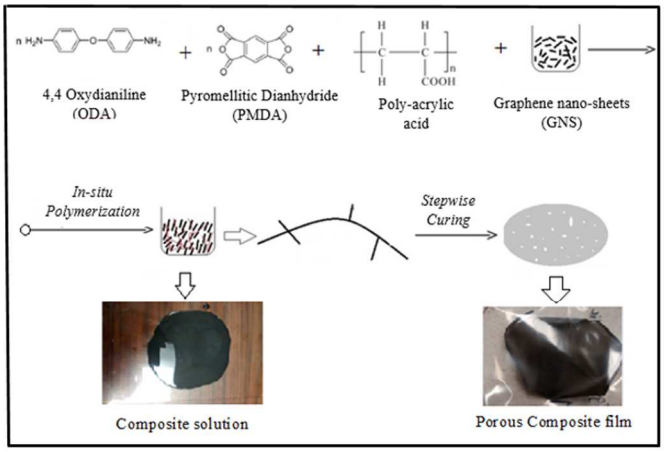

Figure 1a: Schematic illustration of porous graphene/polyimide composite synthesis

2.3 Materials Characterization

2.3.1 Surface area and Pore size measurements

For the BET experiment, composite films are first crushed and weighed, each having a minimum mass of 0.1g and de-gassed in a Micromeritics de-gassing chamber for two hours in nitrogen atmosphere at 150ºC. De-gassing is done to remove trapped moisture and open up pores for better adsorption of nitrogen gas. The samples are re-weighed after de-gassing and the new mass subtracted from the initial weight and placed in the BET chamber for measurement using nitrogen gas as adsorbate. Pore morphology is studied using Phillips XL30 ESEM FEG environmental scanning electron

microscopy. Sample films are cut into thin strips and mounted onto the ESEM electron stage. Secondary electron beams is shot through the samples at different power and magnification and screenshots taken for analysis.

2.3.2 Electrochemical Measurements

The Gamry 9600 Instruments is used for all electrochemical measurements. A two electrode system shown in figure 1b consisting of a working and counter electrodes (positive and negative terminals) with an internal test surface area of 0.850cm^2 is used. 0.4M of potassium hexaflourophosphate VI (KPF_6) dissolved in propylene carbonate is used as electrolyte solution. Potassium hexaflorophosphate VI is selected for this study due to the high mobility and low stoke radius of potassium ions in propylene carbonate (solvated potassium ions have a radius of ~0.426nm in propylene carbonate); this allows ease of penetration of ions through the material. The composite films are cut in small circular sizes of area 0.725cm^2 and mass 0.005g and are swollen for 24 hours in the electrolyte solution to improve wettability. The cell is assembled by inserting two composite films separated by a permeable separator and 0.5ml of the electrolyte solution added in a drop-wise manner. A potential range of -2V to 3.5 V and scan rate of 5mV/s is used for CV experiment, a sinusoidal amplitude voltage of 10mVs rms and an initial and final frequency of 10 Mhz and 0.01Hz respectively is used for the EIS experiment and a voltage range of 0V to 1V and a constant current of 12μA is used for CCD experiment.

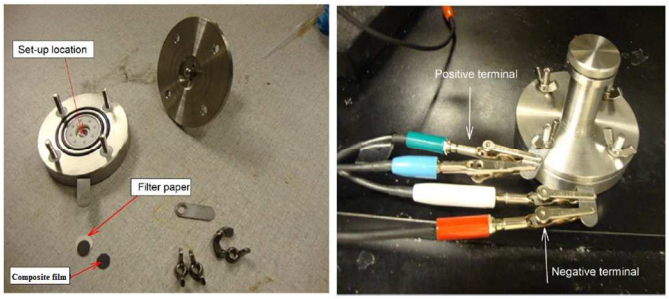

Figure 1b: Two-probe set-up used for electrochemical tests

2.3.3 Structure, Conductivity and Thermal measurements

For these measurements, the composite samples are cut into thin strips. The Renishaw inVia Raman microscope with a laser beam of wavelength λ, 785nm and laser power of 200 mV and an InGaAs detector is used for Raman studies. Fourier transform spectroscopy (FTIR) is carried out using the thermo scientific Nicolet 6700 FT-IR diamond small orbit module, Xray diffraction is done using X'pert Phillips instrument with a monochromatic beam wavelength CuKα = 1.5418Å in a continuous scanning mode, voltage and current of 45kV and 40mA respectively. Xray photospectroscopy (XPS) is carried out using Perkin-Elmer instrument with dual anode x-ray source. Jandel RM3000 four probe test unit is used to measure sheet resistance of sample films with dimensions 2.60cm x 1.0cm x 0.012cm. The probes are first standardized using indium tin oxide (ITO) strip before measurement and a total of three readings are taken. Thermogravrimetric analysis (TGA) is done using TGA Q50 from TA instrument at a heating rate of 10 ^{o}C/min and a temperature scan range of 25 – 800^{o}C in nitrogen atmosphere.

3. Results and discussion

3.1 BET analysis and Morphology studies

The Brunauer, Emmett, Teller (BET) technique calculates surface area (S_{BET}) of a material based on the amount of gas adsorbed on the surface at a given pressure. Figure 2a-d shows BET isotherms for all samples and they exhibit a type IV adsorption/desorption isotherm with a hysteresis due to capillary condensation of adsorbed gas. A little knee between 0 and 0.1Pa represents monolayer adsorption of nitrogen gas in micro-pores while a slight slope in the mid region represents multilayer adsorption of the gas within meso and macro-pores. The adsorption and desorption curves coincides at (P/P_o ~ 0.4) signifying the presence of meso-porous structure nestled in between randomly aligned graphene sheets. Compared to the neat (0%PA), 1%PA, 5wt%PA and 20%PA samples show higher surface areas due to increase in available surface area created by thermally induced pores. Generally, high surface area provides larger area for adsorption and for an electrode material; high surface area is desirable for maximum adsorption of electrolyte species.

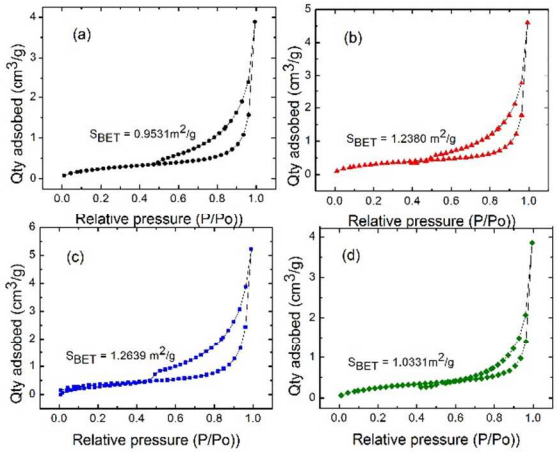

Figure 2: Type IV adsorption/desorption isotherm for (a) 0%PA, (b) 1%PA, (c) 5%PA and (d) 20%PA samples showing measured BET surface area

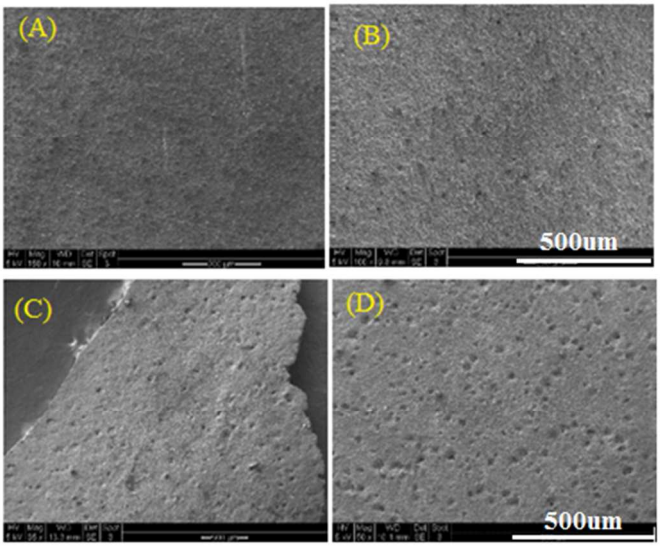

Figure 3(i) a-d: SEM images showing aerial view of 0%PA, 1%PA, 5%PA and 20%PA samples at low magnification

SEM images in figure 3(i-iii) a-d shows pore and surface morphology for each sample. Images taken at very low magnification (figure 3i*a-d*) shows non-uniform porous features on the sample surfaces which are more distinguishable in the 20%PA sample. Images taken at ~2500X (figure 3ii*a-d*) shows finer details with sponge-like interconnected pores more evenly distributed in 1%PA samples. Individual pore morphology can be seen at higher magnification ~8000X (figure 3iii*a-d*) from which pore diameter is measured. The size of the pores depends primarily on the quantity of poly-acrylic resin present in each sample. 1%PA sample synthesized with the lowest weight fraction of poly-acrylic resin show smaller well distributed pores. Its pore distribution allow for better graphene filler dispersion/alignment with fewer aggregates. The 5%PA and 20%PA samples show larger pore sizes due to higher weight fractions of degradable polymer with 20%PA showing very large poorly distributed pores. Compared to the BET, the SEM gives better measurement of the pores primarily because the pores are located on the outer surface. SEM measurements shows show average pore diameter of 2.35µm, 6.02µm and 24.43µm for 1%PA, 5%PA and 20%PA samples respectively. Smaller pores can be created by using lower weight fractions of poly-acrylic resin. Electrochemical measurements is used to study the effect of induced porosity on the ionic mass transport of diffusing species as well as material's energy storage capabilities.

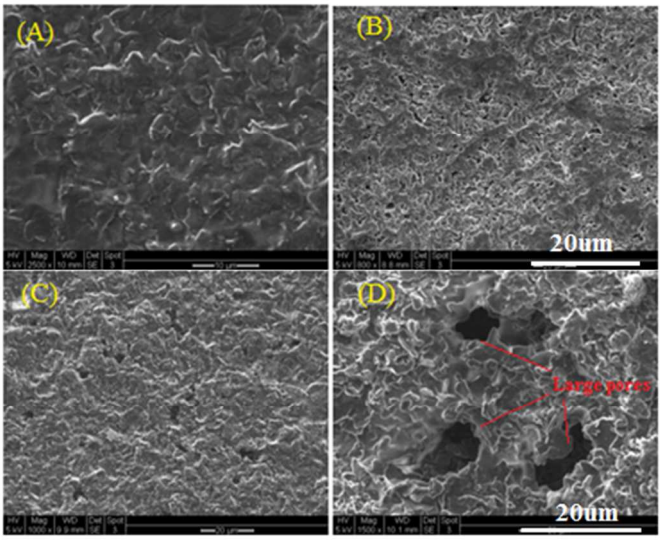

Figure 3(ii) a-d: SEM images showing structural morphology of 0%PA, 1%PA, 5%PA and 20%PA samples at ~2500X magnifications

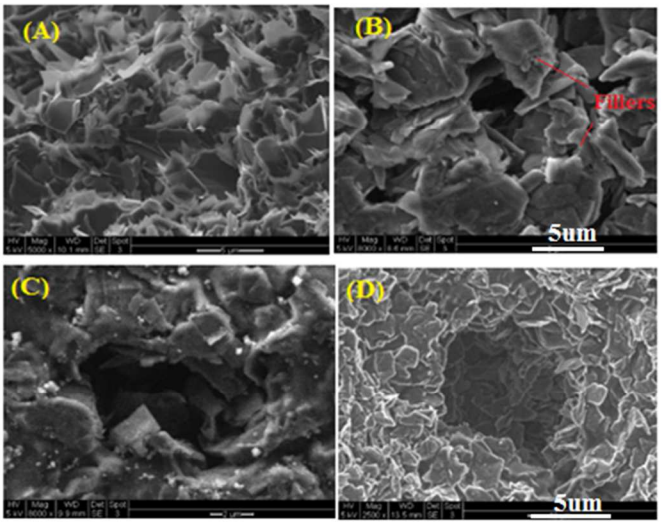

Figure 3(iii) a-d: SEM images showing pore structure of 0%PA, 1%PA, 5%PA and 20%PA samples at ~ 8000X magnification

3.2 Electrochemical measurements

The efficacious exposure of graphene surfaces to electrolyte ions is one of the keys to generating high specific capacitances, however random stacking of the sheets limits surface area available to electrolyte ions thus reducing double layer formation. Pores increase surface area utilization so electrolyte ions have better accessibility to graphene located not only on the outer surface of the material, but also in the inner regions. During degradation, graphene fillers trapped around the poly-acrylic regions loosen and randomly align around created pores. Filler preferred orientation is of great interest while analysing electrochemical behaviour of the composite material, unique ordering causes maximum surface area exposure to diffusing electrolyte ions which increases double layer capacitance. Continuous overlap of filler is observed around the pore regions as shown in the SEM image (figure 3iii). The larger pore diameter of 20%PA sample show higher overlap/stacking of fillers around the pore regions and the non-uniform distribution of pores is due to removal of huge chunks of aggregated resin during curing which limits facile ion transport across pores due to poor pore connectivity. On the other hand, samples synthesized with lower weight fraction of resin (1%PA and 5%PA) yield smaller uniformly distributed pores due to degradation of smaller aggregates of resin within the composite. SEM image for those samples show better well connected pores with improved filler end to end contact. This explains the reason for the slightly higher specific capacitance values observed in samples synthesized with lower resin percent than in 20%PA sample. The rigid non-porous morphology of neat 0%PA sample limits electrolyte contact with embedded fillers thereby causing diffusing ions to be mainly in contact with graphene at the outer regions of the film and not in the bulk.

Unlike planar electrodes, porous electrodes have higher resistances due to cumulative solution resistances. Longer and narrower pores results in more voltage drop down the pore length. The presence of bottlenecks in the pores may decrease penetration depth causing only a small portion of the electrode's surface area to be charged leading to lower capacity values. At lower scan rates, more of the electrode depth is charged hence, higher capacitance values are obtained [20-21]. Cyclic voltammetry (CV), one of the most useful electrochemical techniques is used to acquire qualitative information about electrode/solution interface. CV consists of scanning linearly the potential of a stationary working electrode in an unstirred solution using a rectangular waveform [28]. CV is run at room temperature with a scan rate of 5mv/s in KPF_6/propylene carbonate electrolyte solution. Specific capacitance is determined from voltage window (V_w), measured current (I), scan rate (dV), mass of working electrode (m_{WE}) and potential range (V_f and V_o) [10]

$$C_{sp} = \int_{V_0}^{V_f} \frac{2I}{m_{WE}\, V_w} dV \qquad (1)$$

Figure 4a-b shows a plot of specific capacitance versus number of cycles and CV curves respectively. Specific capacitance is stable across 50 CV cycle runs. The specific capacitance of 1%PA, 5%PA and 20%PA samples are an order of magnitude higher than the neat 0%PA sample due to increased surface area of exposed graphene in the porous regions as earlier explained. A direct correlation is made between capacitance and BET surface area shown in figure 5, specific capacitance increases linearly with BET surface area. This trend is in agreement with what has been widely reported in literature, that specific capacitance increases linearly with specific surface area due to the presence of a larger area available for ion adsorption and separation of

charges [29]. The 5%PA sample with the highest BET surface area has the highest average specific capacitance value of 133.25F/g followed closely by 1%PA with 129.01F/g, 20%PA has a value of 122.5 F/g and the 0%PA sample has the lowest specific capacitance value of 38.94 F/g.

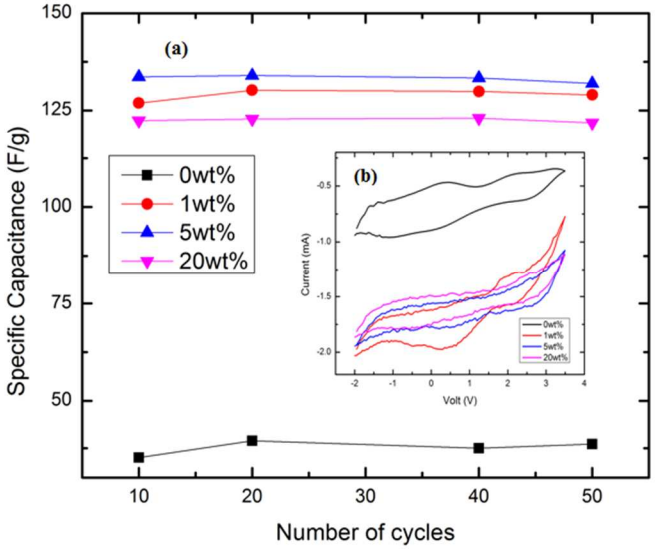

Figure 4: (a) Plot of specific capacitance vs no. of cycles (b) Cyclic voltammogram curves

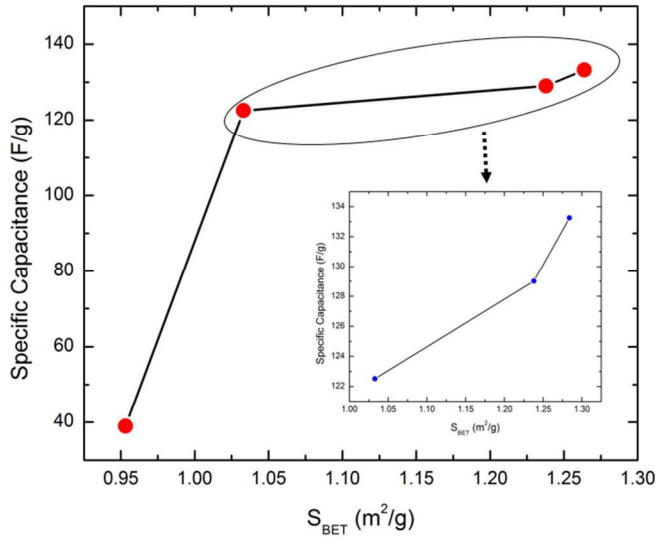

Figure 5: Plot showing relationship between BET surface area and specific capacitance

EIS is used to study mass transport of electrolyte through the material's bulk at varying frequencies. The presence of porous/tortuous network structure increases diffusion resistance and hence affects electrochemical behaviour. To understand this, the complex response of the material to a frequency range of 10 mHz to 1MHz is used for analysis and represented on a nyquist plot with the imaginary impedance plotted against the real impedance. Figure 6a shows nyquist plots for the composite samples. The shape of the nyquist plot is typical for an electrolyte diffusing through a porous medium.

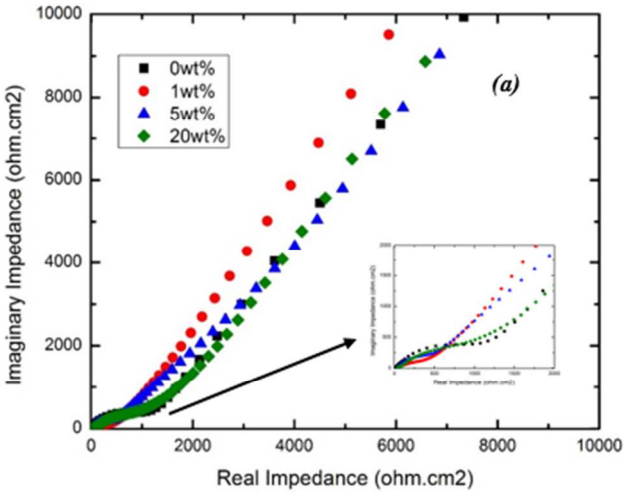

Figure 6a: Nyquist plot showing imaginary vs real impedance

At higher frequencies, resistance and capacitance is low because almost no current flows deep down into the pores of the material [30]. However at low frequencies, diffusion through the bulk is influenced by a Warburg impedance due to distributed resistance and capacitance in the porous electrode and represented as a 45° line with slope ~ 0.5 intercepting the real axis. A purely capacitive behaviour shows a straight vertical line with a slope of 1 however, this system reveals non-ideal capacitive behaviour with associated constant phase element (CPE) impedance given by:

$$Z_{CPE} = \frac{1}{(jw)^{\alpha} Y_o} \qquad (2)$$

where Y_o represents capacitance and α an exponent with values $0 < \alpha < 1$ measuring deviations from ideal capacitive behaviour indicating a distribution of relaxation times due to the effect of pore distribution on electrolyte relaxation [31]. Impedance for an ideally polarizable porous electrode. is given by [32]:

$$Z(w) = \sqrt{\frac{R_w}{jwC}} coth\sqrt{jwR_wC} \qquad (3)$$

where at high frequency, $Z(w \to \infty) = R_w/jwC$; and at low frequency, $Z(0) = 1/jwC$. Total impedance/resistance is summation of ionic resistance

of the bulk electrolyte, the separator material resistance, cell contact resistances and the low frequency resistance. A transmission line model (shown in figure 6b) consisting of Warburg element (W_d) coupled with resistors (R) and constant phase elements (C_{dl}) arranged in series is used to fit data points on the nyquist plots.

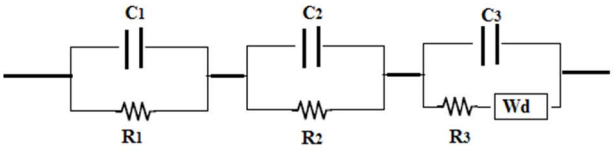

Figure 6b: Transmission line model used for fitting nyquist plots consisting resistors and constant phase elements arranged in series with a Warburg element (W_d)

%PA	Specific capacitance (F/g)	α	Bulk Resistance (kΩ)	Porosity (%)
0	38.94	0.660	0.890	10.42
1	129.01	0.720	0.227	25.90
5	133.25	0.692	0.302	21.50
20	122.51	0.603	0.714	12.09

Table 1: Summary table showing electrochemical results

Results obtained from the fit tabulated on table 1 shows material bulk resistance and deviation parameter (α) for each sample. 1%PA sample exhibits the lowest bulk resistance as well as the least deviation from ideality with a 'α' parameter value of 0.72 due to better transport of electrolyte ions through the material bulk. The material pore morphology and filler orientation seems to enhance ion diffusion due to well-connected porous pathways hence resulting in lower resistances. 5%PA and 20%PA samples show slightly higher resistance than 1%PA possibly due to larger pore sizes which causes aggregation of fillers in pore regions resulting in high material tortuosity. 0%PA sample expectedly has the highest bulk resistance due to its rigid morphology.

Porosity is theoretically estimated from EIS measurements by first calculating effective ionic conductivity (σ_{eff}) using a modified form of Archie's law [33] given by $\sigma_{eff} = t/R_b A$; where R_b is bulk resistance, t is thickness of the sample measured as 0.012cm and A is the contact area of electrode which is 0.725cm^2. Porosity (ϕ_o) is then related to the effective conductivity by $\phi_o = \sqrt[m]{\sigma_{eff}/C\sigma_o}$; where $\mathcal{O}_o$ is electrolyte conductivity given as 6.4mS/m for propylene carbonate, C is the coefficient of saturation ranging from 0.1 to 1 and m is the cementation factor typically in the range of 1.5 to 4 [33]. Calculated porosity values are shown in table 1. 1%PA sample shows the highest porosity which in part explains the reason for its lower resistances. The Cycle life and specific capacity of the composite samples studied using cyclic charge discharge experiment show good capacity retention and cycling stability. Figure 7 shows a plot of log specific capacity vs number of cycles, specific capacity is stable across 100 cycles for all samples. Specific capacity for 1%PA, 5%PA and 20%PA samples is atleast two magnitudes higher than that obtained for the 0%PA sample. This is due to a higher porosity which allows for better capacitive charging within the material's inner creating higher specific capacity. Low porosity of the 0%PA sample only allows a portion of the surface to charge yielding lower capacity.

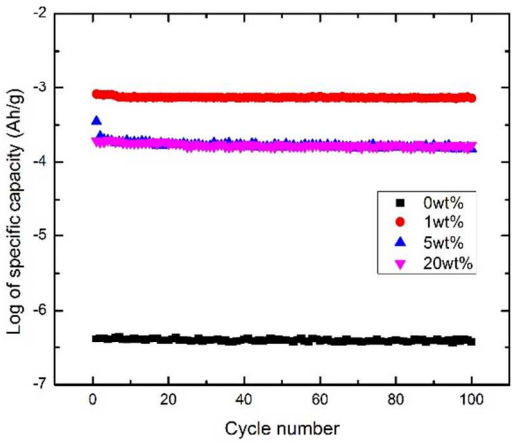

Figure 7: Log of specific capacity vs number of cycles for 100 cycles

3.3 Conductivity measurements

Active graphene fillers exhibit remarkable anisotropic behaviour with respect to electrical conductivity. They are highly conductive in the direction parallel to the graphene layers because of the in-plane metallic

character, whereas exhibit poor conductivity in the direction perpendicular to the layers due to weak van der Waals interactions. Electrical conductivity of free standing graphene prepared by a solvo-thermal reduction of graphene oxide suspension in N-methyl-2-pyrrolidone (NMP) dried at 250°C is 1380S/cm as reported by Chung at al [9]. The presence of functional groups and defects dramatically alters the structure of the carbon plane and affect its conductivity which mainly depend on the long-range conjugated network of the graphitic lattice [42,44]. Functionalization breaks conjugated structure and localizes p-electrons, which results in a decrease of charge carrier. Kumar et al [9] recently reported sheet conductivity of 8.66S/cm for polyaniline grafted graphene composite. The four probe method has been used to estimate sheet conductivity of the samples. Four probe typically measures material's sheet resistance and sheet conductivity calculated from reciprocal of sheet resistivity. Table 2 shows values for sheet resistance and sheet conductivity for the samples. Maximum sheet conductivity obtained is 7.16 S/cm for the 1%PA sample; about twice the value obtained for other samples. This is said to be due to the ordering and orientation of graphene sheets in the sample, the fillers are oriented parallel to the hexagonal plane allowing for ease of electron transport. Sreemanta Mitra et al [43] studied tunnelling conduction of graphene in an insulating polymer matrix. They showed that electrical conductivity arises due to hopping of electrons between localized states provided by the graphene sheets. The close proximity of graphene sheets in 1%PA sample enables fluctuation induced tunnelling of electrons from one sheet to another.

%PA	Sheet Resistance (Ω/Sqr)	Sheet Conductivity (S/cm)
0	22.66	3.15
1	9.97	7.16
5	19.34	3.69
20	28.40	2.52

Table 2: Four probe measurement of sheet resistance and conductivity of samples

3.4 Structure and Compositional analysis

Raman spectroscopy, a useful technique used to observe vibrational, rotational, and other low-frequency modes in a system was used to study composite's interfacial properties. Highly ordered graphite has a couple of Raman-active bands which includes the in-phase vibration of the graphitic lattice G band ($1580cm^{-1}$), a second order overtone of a different in plane vibration ($2690cm^{-1}$) and a first order D band ($1350cm^{-1}$) caused by defects in graphite edges [26-27]. The D band is usually absent for perfect graphite and only becomes prominent due to the presence of sp^3-hybridized carbon atoms present at defects and/or anchor sites of functional groups. The 2D band in functionalized graphene shifts to lower frequencies and narrows compared to that of graphite [28-29]. The presence of functional groups and defects dramatically alters structure of carbon plane and hence affects its properties. Figure 8(ii) shows Raman spectra for all the samples. The characteristic graphitic D, G and 2D bands are observed at lower frequencies $1084cm^{-1}$, $1331.29cm^{-1}$ and $2478.56cm^{-1}$ respectively suggesting interfacial interaction between the polymer matrix and graphene conjugated aromatic rings [19]. Raman spectra for pristine graphene sheets is shown in figure 8(i). 20%PA sample show additional peaks at $1175cm^{-1}$, $1580cm^{-1}$ and $1375.02cm^{-1}$ corresponding to C-C stretching, -COO- asymmetric stretching and -COO- rocking of the carboxylate groups from poly-acrylic acid groups due to the higher content of the resin [38]. Ratio of peak intensities I_D, I_G and I_{2D} relative to one other gives useful information on degree of disorder/defects in graphene basal planes as well as the number of layers of the stacked graphite sheets [34]. The I_D/I_G ratios for 0, 1, 5 and 20% PA samples is 0.288, 0.508, 0.391 and 0.388 respectively. The ratio is higher in 1, 5 and 20% PA samples compared to the 0%PA which confirms successful attachment of poly-acrylic acid chain to graphene during synthesis. The I_{2D}/I_G peak ratios is significantly less than 1 for all the samples, which is due to multilayer graphene sheets (50-100nm) used for experiment. Single or few layer graphene typically have I_{2D}/I_G ratios between 2 and 3.

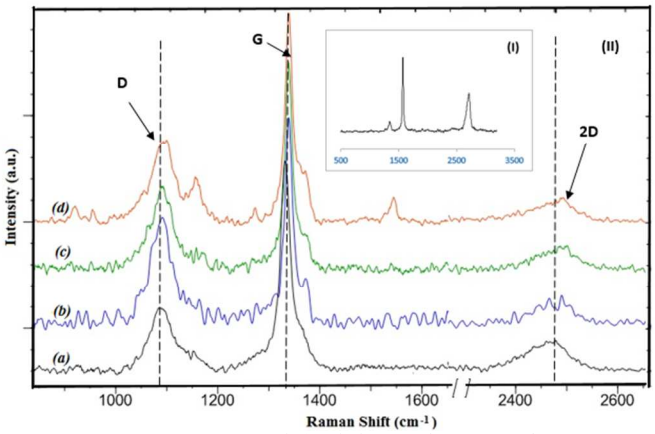

Figure 8: Raman spectra of (I) Pristine graphene nano-sheets (II) graphene/polyimide composite with (a) 0wt% (b) 1wt% (c) 5wt% and (d) 20wt% poly-acrylic content

XRD diffraction spectra (figure 9) shows a sharp intense peak at 2θ angle of about 26.5° corresponding to a d-spacing of 3.36 Å due to inter-planar spacing of the graphene sheets. This suggests the graphitic structure is maintained in all the samples. The peaks become narrower with poly-acrylic content due to increase in grain sizes possibly due to aggregation of sheets. Changes in the peak position is said to be due to interaction between rigid fillers and polymer matrix. Graphene orientation is affected during degradation of soft polymer segment which leads to changes in inter-gallery spacing shown from the slight shift in 2θ peak positions. Schrerrer's equation $L_c = \kappa\lambda/\beta_{001}Cos\theta$ can be used to estimate grain size and the number of graphene sheet grain is calculated using $N_c = L_c/d_{001} + 1$ where $L_c = k\lambda/\beta_{001}Cos\theta$, k=1 and β_{001} is full width at half maximum (FWHM) of the 001 peak in radians. [39]. Average number of sheets per stack is estimated to be between 50 to 100 layers

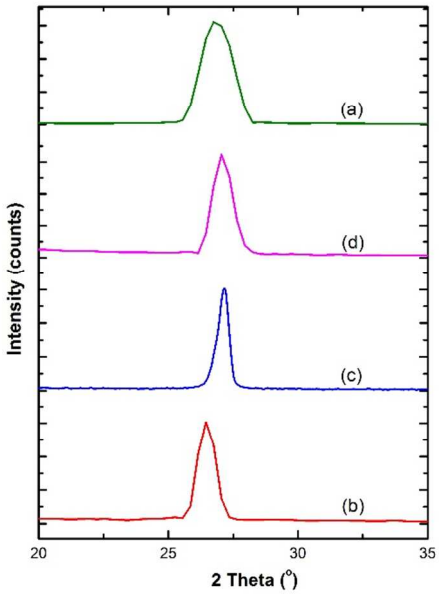

Figure 9a-d: XRD diffraction spectra of (a) 0%PA, (b) 1%PA, (c) 5%PA and (d) 20%PA showing a 2θ angle of ~ 26.5° corresponding to a d spacing of 3.36Å

Compared to Raman, FTIR yields a more meaningful spectra for imide functional groups [40]. Figures 10 (I) and (II) show FTIR spectra for the samples before and after curing. FTIR is used to confirm the presence of chemical interaction/bonding between the phases. Intense peaks observed at 1150cm^{-1} and 1350cm^{-1} in the uncured samples is attributed to stretching of the C-O bond in poly-acrylic acid and is slightly shifted to the left. The presence of multiple peaks at 1720cm^{-1} wavenumber is due to overlap of the carbonyl (C=O) bonds of acrylic group and polyamic acid present. Poly-acrylic resin degradation is tracked using the CO peak at 1150cm^{-1}. Its peak intensity before and after curing at 300°C shows significant decrease by over 80% suggesting successful bond scission of the resin. The characteristic imide peaks become more prominent after curing at 300°C with an out of phase stretching and in phase stretching of the imide carbonyl C=O bond is observed at 1717cm^{-1} and 1774cm^{-1} respectively which is lower than what is typically observed in neat polyimide at 1720cm^{-1} and 1780cm^{-1} respectively. These shifts can be attributed to carbonyl group interaction with filler phase present. Other peaks at 1370cm^{-1} and 1500cm^{-1} are due to the stretching of the imide C-N bond and the benzene ring respectively. A graphitic peak is observed at 1175cm^{-1} and the one at 1694cm^{-1} is overlapped by the imide

carbonyl peak at 1717 cm^{-1} further confirming interfacial interaction between the filler and polymer matrix phase.

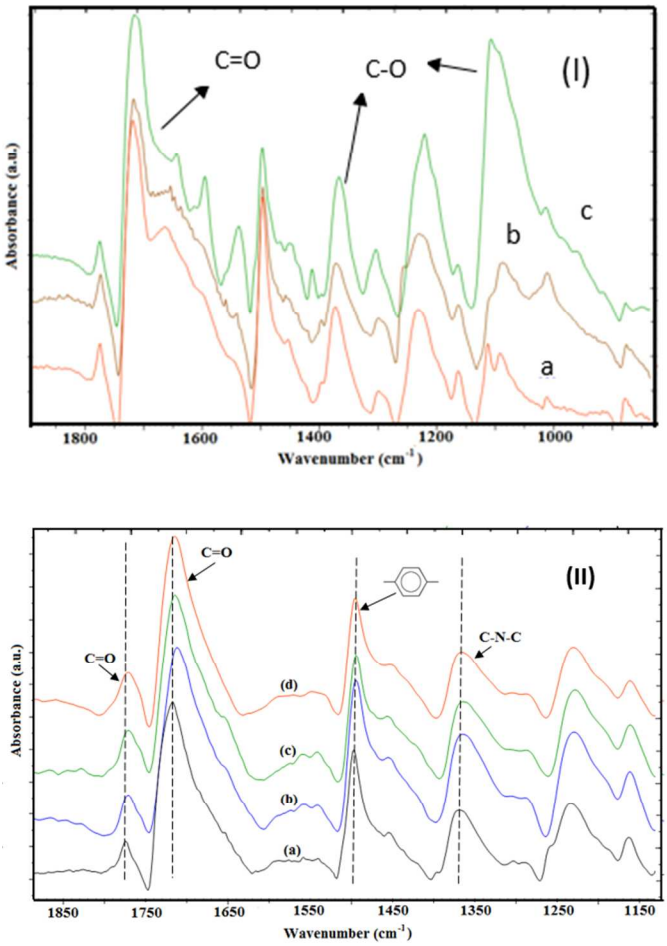

Figure 10: FTIR spectra (I) before curing for (a) 1%PA (b) 5%PA (c) 20%PA samples and (II) after curing at 300°C for (a) 0%PA (b) 1%PA (c) 5%PA and (d) 20%PA samples

X-ray photoelectron spectroscopy (XPS) was used for surface analysis. Bleda-Martinez et al [26] demonstrates the effect of surface chemistry on double layer capacitance. Oxygen atoms bonded to CO– groups are shown to contribute to higher capacitance values observed for activated carbon materials. Quantitative elemental analysis tabulated in table 3 show changes to surface chemistries of the samples due to variations in C/N and C/O ratios with increasing poly-acrylic content. It is suspected that bond scission of the acrylic bonds introduces more CO- groups into the system thereby partly contributing to higher specific capacitance values observed for those samples. Further studies however needs to be carried out to ascertain this.

	Atom %		
%PA	C 1s	O 1s	N 1s
0	70.341	18.141	4.094
1	65.549	20.071	4.150
5	56.686	25.215	3.921
20	49.486	28.778	3.215

Table 3: Summary table showing C, N and O elemental composition of composites

De-convoluted carbon 1s peak (figure 11) show peaks at several binding energies, the characteristic intense peak at 284.5eV is mainly due to carbon atoms attached to C-C bond, peaks at higher binding energies suggests the presence of oxidized carbon atoms, C=O at 288.4eV (which are from carbonyl and quinone), C-O-C and C-OH at 286.1eV. The phenyl imide carbon atom C-N is seen at a binding energy of 285eV. Additional peaks at 289.1eV and 289.3eV binding energies seen in samples containing poly-acrylic acid corresponds to O-C=O and OH-C=O due to poly-acrylic acid functionalities while peak at 283eV is attributed to a carbon impurities.

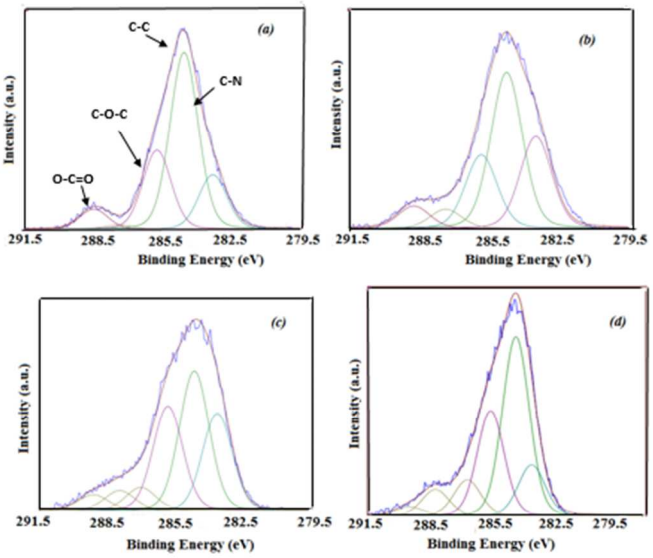

Figure 11: *De-convoluted carbon peak for (a) 0%PA, (b) 1%PA, (c) 5%PA and (d) 20%PA samples*

3.5 **Thermal analysis**

Poly-acrylic resin degradation was studied using the TGA. Figure 12a-b shows TGA and derivative TGA plots for sample weight loss between 25°C and 800°C. Changes to slope in TGA curve as well as presence of multiple peaks in the DTG curve shows degradation is a multi-step process. Initial weight loss of about 1-2wt% observed between 50°C and 100°C is attributed to trapped moisture and other volatiles within the composites while a weight loss of about 2-8% between 100°C and 200°C is attributed to evaporation of residual NMP solvent used in the reaction. Onset of poly-acrylic acid degradation starts from about 275°C (poly-acrylic degradation starts at 200°C in air [45]) with 100% weight loss observed at 350°C for the neat poly-acrylic sample as seen from the TGA plot. The total amount of acrylic phase leached out from the samples at the curing conditions employed during preparation of samples (300°C for 4 hours in vacuum) is expected to be slightly higher than the TGA results at the same temperature because of 'temperature-pressure' effect as well as heating rate. Degradation occurs mainly by unzipping of the alpha carbon bond to form low molecular weight volatile organics. Over 10% weight loss is observed between 200°C and 350°C in 1%PA, 5%PA and 20%PA samples with complete degradation of the poly-acrylic phase at higher temperatures between 350°C and 550°C due to a higher activation energy required to break interfacial bond present. Extent of weight loss is approximately equal to the amount of acrylic polymer in the composites with 20wt% sample showing the highest weight loss of about 20% at 550°C. Neat polyimide (PI) and pristine graphene nano-sheets (GNS) show high thermal stability up to 700°C.

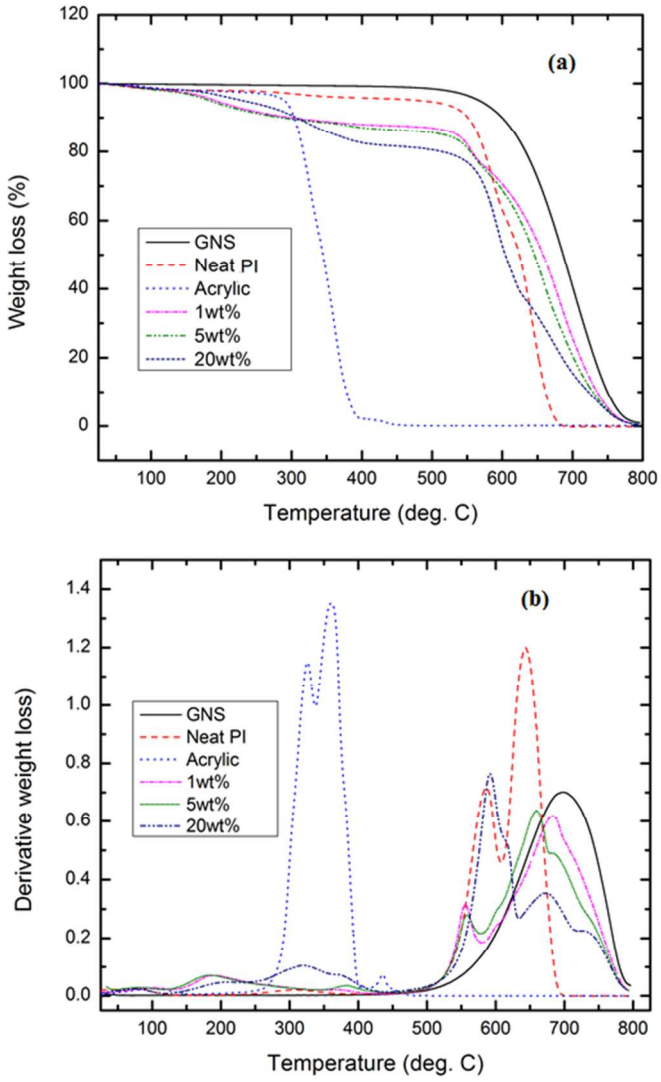

Figure 12: TGA plot showing (a) Weight loss versus temperature and (b) Derivative weight loss versus temperature

4.0 Conclusion

Porous graphene-polyimide composite films synthesized by thermal degradation of grafted poly-acrylic leachable phase was studied. The electrochemical behaviour of the system is greatly improved due to changes to the material's morphology and surface characteristics. Induced porosity improved filler available surface area, enhanced wettability/diffusion of ionic species from the surface to the bulk of the material and yielded enhanced double layer capacitance. A direct correlation is seen between pore size and electrochemical properties, smaller sized pores produced higher capacitances due to better pore distribution which enhances facile ion transport between pores and

material bulk. Compared to neat graphene-polyimide composite, the samples synthesized with poly-acrylic resin showed better overall improved properties. Structural analysis reveals the formation of a homogeneous composite system with strong interfacial bonds between the phases. Further pore size tuning is expected to significantly increase material's electrochemical behaviour.

.

Acknowledgements

Financial support is provided by University of Cincinnati's seed fund. Characterization is carried out at the advanced material's characterization center (AMCC), department of chemistry and the advanced polymer and composites laboratory, University of Cincinnati, Cincinnati, Ohio.

Notes and references

[1] G. A. Snook, P. Kao, and A. S. Best, *J. Power Sources*, vol. 196, no. 1, pp. 1–12, 2011.

[2] C. Peng, S. Zhang, D. Jewell, and G. Z. Chen, *Progress Nat. Sci.*, vol. 18, pp. 777–788, 2008.

[3] E. Frackowiak, V. Khomenko, K. Jurewicz, and K. Lota, *J. Power Sources*, vol. 153, pp. 413–418, 2006.

[4] L. L. Zhang, R. Zhou, and X. S. Zhao, *J. Mater. Chem.*, pp. 5983–5992, 2010.

[5] F. Fabregat-santiago, A. Compte, and J. Bisquert, *Electrochem. Commun. 1 (1999) 429–435*, vol. 1, pp. 429–435, 1999.

[6] P. Pieta, I. Obraztsov, F. D'Souza, and W. Kutner, *ECS J. Solid State Sci. Technol.*, vol. 2, no. 10, pp. M3120–M3134, Sep. 2013.

[7] J. Xia, F. Chen, J. Li, and N. Tao, *Nat. Nanotechnol.*, vol. 4, no. 8, pp. 505–9, Aug. 2009.

[8] J. Liu, *Nat. Nanotechnol.*, vol. 9, no. 10, pp. 739–741, Oct. 2014.

[9] K. Singh, A. Ohlan, and S. K. Dhawan, *Intech*, pp. pp. 37–71, 2012.

[10] B. Dyatkin and Y. Gogotsi, *Faraday Discuss.*, vol. 172, pp. 139–162, 2014.

[11] Y. Wang, Z. Shi, Y. Huang, Y. Ma, C. Wang, M. Chen, and Y. Chen, *J. Phys. Chem.*, pp. 13103–13107, 2009.

[12] Z. Song, T. Xu, M. L. Gordin, Y. Jiang, I. Bae, Q. Xiao, H. Zhan, J. Liu, and D. Wang, *Nano Lett.*, 2012.

[13] C. Z. Xin Fang, Mingyuan Ge Jiepeng Rong, *Journals Mater. Chem.*, vol. Vol. 1, no. Issue 12, pp. pp. 4083–4088.

[14] V. Murugan, T. Muraliganth, and A. Manthiram, *Chem. Mater.*, vol. 21, no. 21, pp. 5004–5006, Nov. 2009.

[15] A. Georgiev, D. Dimov, E. Spassova, J. Assa, P. Dineff, and G. Danev, *Intech*, pp. pp. 66–84, 2012.

[16] V. Ratieuville, K. Fatyeyeva, C. Chappey, S. Rogalskyy, O. Tarasyuk, and S. Marais, *Adv. Mater. Res.*, vol. 747, pp. 477–480, Aug. 2013.

[17] D. A. S. et al Mitra Yoonessi, Ying Shi, *ACS Nano*, vol. Vol. 6, no. Issue 9, pp. pp. 7644–7655., 2012.

[18] Y. Tao, X. Xie, W. Lv, D.-M. Tang, D. Kong, Z. Huang, H. Nishihara, T. Ishii, B. Li, D. Golberg, F. Kang, T. Kyotani, and Q.-H. Yang, *Sci. Rep.*, vol. 3, p. 2975, Jan. 2013.

[19] Y. Meng, H. Wu, Y. Zhang, and Z. Wei, *J. Mater. Chem. A*, vol. 2, no. 28, p. 10842, 2014.

[20] S. M. and K. M. A. Cormac O. Laoire, *J. Phys. Chem.*, vol. Vol. 114, pp. pp. 9178–9186, 2010.

[21] Y. G. and C. Largeot, C. Portet, J. Chmiola, P. L. Taberna and P. Simon, *J. Am. Chem. Soc.,* vol. 130, pp. 2730–2731.

[22] K. Kinoshita, Wiley-Interscience, New York (1988)., 1988.

[23] B.E.Conway, Kluwer Academy/Plenum Publisher, 1999.

[24] A. Yoshida, I. Tanahashi, and A. T. U. Nishino, *Carbon N. Y.*, vol. 28, no. 5, pp. 611–615, 1990.

[25] W. E. T. Al, *ACS Nano*, no. 3, pp. 2422–2430, 2013.

[26] M. J. Bleda-Martínez, J. a. Maciá-Agulló, D. Lozano-Castelló, E. Morallón, D. Cazorla-Amorós, and a. Linares-Solano, *Carbon N. Y.*, vol. 43, no. 13, pp. 2677–2684, Nov. 2005.

[27] Avinash Balakrishnan. K. R. V. Subramanian, Boca Raton, FL: CRC Press, 2014.

[28] L. R. F. Allen J. Bard, 2nd Ed. John Wiley & Sons, Inc., 2001.

[29] F. Lufrano, P. Staiti, T. Avanzate, and E. Nicola, *Int. J. Electrochem. Sci.*, vol. 5, pp. 903–916, 2010.

[30] R. Ko and M. Carlen, *Electrochem. Acta*, vol. 45, pp. 2483–2498, 2000.

[31] B. Batalla García, A. M. Feaver, Q. Zhang, R. D. Champion, G. Cao, T. T. Fister, K. P. Nagle, and G. T. Seidler, *J. Appl. Phys.*, vol. 104, no. 1, p. 014305, 2008.

[32] P. D. (ed. . R. De Levie, Vol. 6,. New York: Interscience Publishers, 1967, p. pp. 329.

[33] S. Tully-dartez, H. E. Cardenas, D. Ph, and P. S. Sit, *Tissue Eng.*, vol. 16, no. 3, 2010.

[34] I. Childres, L. A. Jauregui, W. Park, H. Cao, and Y. P. Chen, "Raman Spectroscopy of graphene and related materials," .

[35] Yan Wang, Zixing Shi, Jianhua Fang, Hongjie Xue, *J. Mater. Chem.*, vol. Vol. 21, pp. pp. 505–512, 2011.

[36] G. P. and N. T. Anastasios Stergiou, *J. Nanotechnol.*, vol. vol. 5, pp. 1580–1589, 2014.

[37] C. N. L. Calizo, A. A. Balandin, W. Bao, F. Miao, *Nano Lett.*,. Vol. 7, no. Issue. 9, pp. pp. 2645–2649, 2007.

[38] D. . W. A.M Young, A Sherpaa, G Pearson, B Schottlander, *Biomaterials*, vol. Volume 21, no. Issue 19, p. Pages 1971–1979.

[39] J. Longun and J. O. Iroh, *Carbon N. Y.*, vol. 50, no. 5, pp. 1823–1832, Apr. 2012.

[40] J. J. Ge, G. Xue, F. Li, K. W. Mccreight, S. Wang, F. W. Harris, S. Z. D. Cheng, X. Zhuang, S. Hong, and Y. R. Shen, vol. 623, no. 12, pp. 619–623, 1998.

[41] A. O. D. Lozano-Castelló, D. Cazorla-Amorós, A. Linares-Solano, S. Shiraishi, H. Kurihara, " *Carbon N. Y.*, vol. vol. 41, no. no. 9, pp. pp. 1765–1775, 2003.

[42] K. Spyrou and P. Rudolf, 2014.

[43] S. Mitra, S. Banerjee, and D. Chakravorty, *J. Appl. Phys.*, vol. 113, no. 15, p. 154314, 2013.

[44] G. R. Ruschau and R. E. Newnham, *J. Compos. Mater.*, vol. 26, no. 18, pp. 2727–2735, Jan. 1992.

[45] W.-C. Wang, R. H. Vora, E.-T. Kang, K.-G. Neoh, C.-K. Ong, and L.-F. Chen, *Adv. Mater.*, vol. 16, no. 1, pp. 54–57, Jan. 2004.

GRAPHICAL ABSTRACT

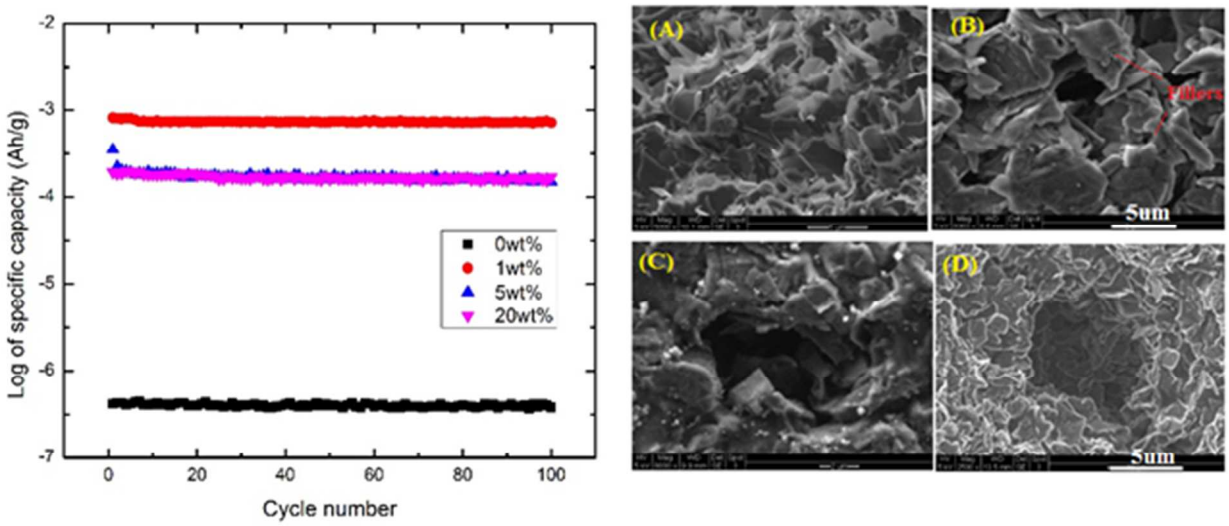

A plot of log specific capacity versus number of cycles for graphene-polyimide composite samples and their SEM images